

Gravitational signals due to tidal interactions between white dwarfs and black holes

C. Casalbieri¹, V. Ferrari¹, A. Stavridis²

¹ *Dipartimento di Fisica “G.Marconi”, Università di Roma “La Sapienza”*

and Sezione INFN ROMA1, piazzale Aldo Moro 2, I-00185 Roma, Italy

² *Department of Physics, Aristotle University of Thessaloniki, Thessaloniki 54006, Greece*

12 November 2018

ABSTRACT

In this paper we compute the gravitational signal emitted when a white dwarf moves around a black hole on a closed or open orbit using the affine model approach. We compare the orbital and the tidal contributions to the signal, assuming that the star moves in a safe region where, although very close to the black hole, the strength of the tidal interaction is insufficient to provoke the stellar disruption. We show that for all considered orbits the tidal signal presents sharp peaks corresponding to the excitation of the star non radial oscillation modes, the amplitude of which depends on how deep the star penetrates the black hole tidal radius and on the type of orbit. Further structure is added to the emitted signal by the coupling between the orbital and the tidal motion.

Key words: gravitational waves — stars: oscillations — relativity — stars:white dwarfs

1 INTRODUCTION

Recent astronomical observations have shown evidence of interactive processes in action between stars and black holes. The ESO Very Large Telescope (VLT) has observed stars that move on very elliptic orbits around the supermassive black hole at the center of our Galaxy (Schodel *et al.* 2002), and X-ray satellite CHANDRA has monitored the event of a star disrupted and swollen by the giant black hole at the center of the galaxy RXJ1242-11 (Komossa *et al.* 2004). These and similar phenomena that take place around black holes

generate gravitational waves essentially because of two mechanisms: one related to the time variation of the quadrupole moment of the system star-black hole due to the orbital motion, the second to the quadrupole moment of the star which changes in time because the star is deformed by the tidal interaction with the black hole. The orbital contribution has been computed using the Post-Newtonian formalisms (see for instance (Blanchet 2002) and references therein). In this paper we shall focus on the second mechanism: we shall consider a white dwarf (WD) moving on assigned orbits around a black hole (BH), we shall compute how the stellar shape and structure change along its motion and the gravitational wave (GW) signal emitted due to this time-varying deformation.

The problem of tidal deformation has been widely investigated both in newtonian gravity and in general relativity, using different approaches.

In 1977 Press and Teukolsky studied the formation of binary systems by two-body tidal capture using a perturbative approach and provided estimates of the amount of orbital energy absorbed in the encounter (Press & Teukolsky 1977).

In the early eighties a formalism was developed (Carter & Luminet 1982; Carter & Luminet 1983; Carter & Luminet 1985) that allows to compute the tidal deformation by integrating a set of equations which describe the motion of an element of stellar fluid due to the effect of the tidal tensor of the other massive body, on the assumption that while deforming the star maintains an ellipsoidal form (affine model). This approach, initially developed in the framework of Newtonian gravity, was subsequently generalized to general relativity when one of the interacting bodies is a Schwarzschild or a Kerr black hole (Marck 1983; Luminet & Marck 1985). The affine model has been used in several papers addressing some relevant astrophysical problems: in (Luminet & Carter 1986; Luminet & Pichon 1989; Bicknell & Gingold 1983) the authors investigated whether, in the interaction with a massive companion, a main sequence (MS) star can be compressed to such an extent that the temperature increase in the core can ignite a detonation of the nuclear fuel (a process which may occur in active galactic nuclei having a central massive black hole); the tidal capture of a main sequence star and its disruption have been investigated in (Carter 1992) and in (Kochanek 1992), respectively; tidal processes occurring in neutron star-neutron star coalescing binaries before contact has been investigated in (Kochanek 1992), where the phase shift induced on the emitted gravitational signal has also been computed; the chemical and mechanical behaviour of a WD passing inside the tidal radius of a black hole has been studied in (Luminet & Pichon 1989); furthermore, the affine model has also been used in

(Kosovichev & Novikov 1992; Diener *et al.* 1995) to study the tidal capture and interaction of a star and a massive BH.

Tidal effects in close compact binaries have also been studied using different formalisms; for instance, by integrating the hydrodynamical equations in 3D, in a form adapted to express the evolution of the star principal axes and of other relevant quantities, and including radiation reaction and viscous dissipation (Lai, Rasio & Shapiro 1993; Lai, Rasio & Shapiro 1994; Lai, Rasio & Shapiro 1994; Rasio & Shapiro 1995; Lai, Rasio & Shapiro 1995). An alternative approach to the integration of the 3D-hydrodynamical equations has been used in (Frolov *et al.* 1984) to study disruptive and non disruptive encounters between white dwarfs and black holes, focusing on the determination of the periastron distance, time delay, relativistic precession and tidal forces.

Further studies on tidal interactions in close binaries are in (Evans & Kochanek 1989; Novikov, Pethick & Polnarev 1992; Laguna *et al.* 1993; Khokhlov, Novikov & Pethick 1993; Khokhlov, Novikov & Pethick 1993; Ogawaguchi & Kojima 1996; Marck, Lioure & Bonazzola 1996; Diener *et al.* 1997; Fryer *et al.* 1999; Ferrari, D’Andrea & Berti 2000; Shibata & Uryu 2001; Gualtieri *et al.* 2001; Berti & Ferrari 2001; Ivanov & Novikov 2001; Pons *et al.* 2002; Ivanov, Chernyakova & Novikov 2003; Gomboc & Cadez 2005).

In this paper we use the Carter-Luminet approach to study the tidal interaction of a white dwarf and a black hole, with the purpose of computing the gravitational signal emitted in this process. We shall integrate the Carter-Luminet equations for open and closed orbits choosing a white dwarf mass $M_* = 1 M_\odot$ and a black hole mass $M_{BH} = 10 M_\odot$. The WD will be modeled using a polytropic equation of state (EOS) with adiabatic index $\gamma = 5/3$. The gravitational radiation will be computed by using the quadrupole approach and the orbital and the tidal contributions will be compared. We shall further discuss how the results change for higher values of the black hole mass.

Our study is based on several simplifying assumptions:

- The WD mass is assumed to be much smaller than the black hole mass.
- The black hole does not rotate and the equations of motion of the star, its internal structure and the black hole tidal tensor are computed using the equations of newtonian gravity; thus, we call “black hole” an object which is basically a point mass star. We plan to extend our calculations to general relativity and to rotating black holes in the near future.
- We neglect tidal effects on the orbital motion.

- We neglect viscous effects, an hypothesis which appears to be justified in the case of WD-BH binaries (Wiggins & Lai 2001).

The plan of the paper is the following. In section 2 we summarize the equations we use to compute the tidal deformation of the star in the affine model approach, and those needed to compute the emitted radiation. In section 3 we discuss the results of our study: for the $1 M_{\odot} - 10 M_{\odot}$ WD-BH binary we compare the orbital and the tidal contributions to the gravitational signal, for circular, elliptic and parabolic orbits; we further discuss how these results depend on the black hole mass. Conclusions are drawn in section 4.

2 THE RELEVANT EQUATIONS

As mentioned in the introduction, the equations we use to describe the tidal deformation of the star are fully Newtonian, and have been developed in (Carter & Luminet 1982; Carter & Luminet 1983; Carter & Luminet 1985).

Let us consider a spherical star with mass M_* and radius R_* in equilibrium, and be \hat{r} the Cartesian position vector of the generic fluid element with respect to a frame relative to the center of mass of the star in this unperturbed configuration. To hereafter, the ‘hat’ will indicate quantities computed in this frame for the unperturbed star.

We shall assume that the star is composed of a perfect fluid with a polytropic EOS

$$P = K\rho^{\gamma}. \quad (1)$$

M_* will move on assigned orbits around a non rotating, massive body $M_{BH} \gg M_*$, to which we associate a reference frame \mathcal{O}_{BH} . Be $\vec{X}(t)$ the vector which identifies the position of the center of mass of the star with respect to this frame.

While moving around M_{BH} , the star is deformed by the tidal interaction, and we shall indicate as \mathcal{O}_* the reference frame relative to the center of mass of the moving star in a parallel propagated frame; in this frame, the position of each fluid element will be given by the vector $\vec{r}(t)$. Thus, the position of the generic fluid element of the star with respect to \mathcal{O}_{BH} will be

$$x_i = X_i + r_i, \quad (2)$$

and \vec{r} will be a function of time, related to \hat{r} by

$$\vec{r}_i = q_{ij}\hat{r}_j \quad (i, j = 1, 2, 3) \quad (3)$$

where q_{ij} is a 3×3 uniform matrix, i.e. it depends on time but it is independent of r , which

implies that the star can assume only *ellipsoidal* configurations (affine model). q_{ij} is the matrix we need to compute to know how the stellar shape changes along the orbit.

Under the assumption of polytropic EOS, the q_{ij} satisfy the following equations (Carter & Luminet 1983)

$$\ddot{q}_{ij} = C_{ik}q_{kj} + \frac{\Pi_*}{\mathcal{M}_*} \left[\frac{\Pi}{\Pi_*} q_{ji}^{-1} - \frac{3}{2} \int_0^\infty du \frac{(S + uI)_{ni}^{-1}}{\Delta} q_{nj} \right], \quad (4)$$

where

$$C_{ij} = -\frac{\partial^2 \Phi_E}{\partial X_i \partial X_j} \quad (5)$$

is the black hole tidal tensor computed from the Newtonian potential

$$\Phi_E = \frac{GM_{BH}}{X}. \quad (6)$$

In eqs. (4) Π is the volume integral of the local pressure

$$\Pi \equiv \int P \cdot dV, \quad (7)$$

and, since

$$\rho = \hat{\rho} \cdot ||q||^{-1}, \quad (8)$$

where $\hat{\rho}$ is the density in the spherical unperturbed configuration and $||q|| \equiv \det q$, it can be written as

$$\Pi = K \int \rho^\gamma dV = K ||q||^{1-\gamma} \int \hat{\rho}^{\gamma-1} dM = ||q||^{1-\gamma} \int \hat{P} dV \equiv \Pi_* ||q||^{1-\gamma}. \quad (9)$$

Π_* is the value of Π in the unperturbed configuration. Furthermore, \mathcal{M}_* is the scalar quadrupole moment of the initial configuration

$$\mathcal{M}_* = \frac{1}{3} \int \hat{r}_i \hat{r}_i dM. \quad (10)$$

The function Δ in eq. (4) is

$$\Delta = \sqrt{||S + uI||}, \quad (11)$$

where I is the identity matrix,

$$S_{ij} = q_{ik}q_{jk}, \quad (12)$$

and u is the integration variable of the integral appearing in (4).

If the star is initially non rotating (as we shall assume), or if its initial spin is orthogonal

to the orbital plane, the non vanishing components of q_{ij} reduce to (Carter & Luminet 1983)

$$q_{ij}(t) = \begin{pmatrix} q_{11} & q_{12} & 0 \\ q_{21} & q_{22} & 0 \\ 0 & 0 & q_{33} \end{pmatrix}. \quad (13)$$

2.1 Gravitational radiation

The gravitational signal emitted by the system will be computed by using the quadrupole formalism, according to which

$$\begin{cases} h_{\mu 0}^{TT} = 0 & \mu = 0, 3 \\ h_{ik}^{TT}(t, r) = \frac{2G}{c^4 r} \left[\frac{d^2}{dt^2} m_{ik}^{TT} \left(t - \frac{r}{c} \right) \right] \end{cases} \quad (14)$$

where m_{ij}^{TT} is the source quadrupole moment projected on the **TT**-gauge

$$m_{ij}^{TT} = \mathcal{P}_{ijlm} m_{lm} \quad (15)$$

and \mathcal{P}_{ijlm} is the projector tensor. For the system under consideration, the quadrupole moment can be evaluated as follows

$$m_{ik}(t) = \frac{1}{c^2} \int_V T^{00}(t, x_j) x_i x_k d^3x \equiv \int_V \rho(t, r_j) (X_i + r_i) (X_k + r_k) d^3r, \quad (16)$$

i.e.

$$\begin{aligned} m_{ik}(t) &= \int_V \rho(t, r_j) X_i(t) X_k(t) d^3r + \int_V \rho(t, r_j) r_i r_k d^3r \\ &+ X_i(t) \int_V \rho(t, r_j) r_k d^3r + X_k(t) \int_V \rho(t, r_j) r_i d^3r, \end{aligned} \quad (17)$$

where we remind that the $X_i(t)$ are the coordinates of the center of mass of the star with respect to \mathcal{O}_{BH} , whereas $r_k(t)$ are the coordinates of the element of stellar fluid with respect to \mathcal{O}_* . The first integral is the standard quadrupole moment associated to the orbital motion

$$m_{ik}^{orb}(t) = X_i(t) X_k(t) \int_V \rho(t, r_j) d^3r = M_* X_i(t) X_k(t). \quad (18)$$

The second integral is the contribution due to the tidal interaction which, using eqs. (3) can be written as

$$m_{ik}^{def}(t) = \int_V \rho(t, r_j) r_i r_k d^3r = q_{il}(t) q_{km}(t) \int_V \hat{\rho}(t, \hat{r}_j) \hat{r}_l \hat{r}_m d^3\hat{r}. \quad (19)$$

In the last equality we have used eq. (8) and the property that the volume scales as

$$d^3r = ||q|| d^3\hat{r}. \quad (20)$$

Using eqs. (10) and (12), eq. (19) becomes

$$m_{ik}^{def}(t) = q_{il}(t) q_{km}(t) \int_V \hat{r}_l \hat{r}_m dM = \mathcal{M}_* S_{ik}(t). \quad (21)$$

Table 1. The limiting value of β above which the tidal interaction between the white dwarf and the black hole becomes disruptive is given for the orbits considered in this paper.

Orbit	e	β_{crit}
Circular	0	0.78
Parabolic	1	1.05
Elliptic	0.25	0.78
	0.75	0.97
	0.95	1.03

The last two integrals in (16) vanish due to symmetry; indeed

$$X_i(t) \int_V \rho(t, r_j) r_k d^3r = X_i(t) q_{km}(t) \int_V \hat{\rho}(t, \hat{r}_j) \hat{r}_m d^3\hat{r} = 0 \quad (22)$$

since for every fluid element that, in the unperturbed configuration, has coordinates $r_j = (x_j, y_j, z_j)$ there exists one with coordinates $(-x_j, -y_j, -z_j)$. Thus, in conclusion, the quadrupole moment of the system is composed of two contributions, the orbital one, m_{ik}^{orb} (eq. 18), and that due to the tidal interaction, m_{ik}^{def} (eq. 21).

3 RESULTS

Eqs. (4) have been integrated for a system composed of a white dwarf described by a polytropic EOS with $\gamma = \frac{5}{3}$ and a more massive companion of mass $M_{BH} = 10 M_\odot$. The WD central density of the unperturbed configuration is such that $M_* = 1 M_\odot$ and $R_* = 6955 \text{ km}$.

We have considered circular, elliptic and parabolic orbits, and using eqs. (18), (21) and (14) we have computed the emitted gravitational signal.

It is known that if the periastron of the orbit lays within a certain critical radial distance from M_{BH} the star can be destroyed by the tidal interaction. This radius, R_R , mainly depends on the composition of the interacting bodies and on the orbit. According to Newtonian Gravity R_R is approximately

$$R_R \approx \left(\frac{M_{BH}}{\bar{\rho}} \right)^{\frac{1}{3}} \approx \left(\frac{M_{BH}}{M_*} \right)^{\frac{1}{3}} R_*, \quad (23)$$

where $\bar{\rho}$ is the star average density. As usual, we define a penetration factor as the ratio

$$\beta = \frac{R_R}{R_p}, \quad (24)$$

where R_p is the distance of closest approach between the two bodies.

In order to establish what is the critical value of β below which the star can safely

approach the black hole without being destroyed by the tidal interaction, we proceed as follows. We monitor the behaviour of the star principal axes as a function of time for increasing values of β . As an example, in figure 1 we plot the axes for two parabolic orbits corresponding to $\beta = 1$ (upper panel) and $\beta = 1.1$ (lower panel log-scale). In the first case the axes oscillate around average values that approximately correspond to a conformal Riemannian stationary configuration (Diener *et al.* 1995). Conversely, for $\beta = 1.1$ we see one axis indefinitely growing, and this signals a destructive interaction. In table 1 we give the values of β_{crit} for circular, elliptic and parabolic orbits for the system we consider. β_{crit} is the limiting value of β above which we observe the indefinite growing of one axis.

In what follows we shall consider only values of $\beta \leq \beta_{crit}$. In all cases we shall assume that the orbit lays on the equatorial plane ((x, y) -plane) and we shall compute the gravitational signal emerging in the z -direction in the **TT**-gauge. h_+^{def} and h_\times^{def} will refer to the part of the signal due to the tidal interaction and to the consequent stellar deformation, computed using the quadrupole moment (21), whereas h_+^{orb} and h_\times^{orb} will be the orbital contribution, computed using eq (18).

3.1 Circular orbits

When the orbit is circular, the orbital contribution to the gravitational signal is

$$h_+^{orb}(t) = ih_\times^{orb}(t) = A \frac{\cos(2\omega_{orb}t)}{r}, \quad (25)$$

where $\omega_{orb} = \left(\frac{GM}{D^3}\right)^{1/2}$ is the Keplerian angular velocity, D being the separation between the two bodies, r is the radial distance from the source, and

$$A = \frac{4G^2 M \mu}{c^4}, \quad (26)$$

where $M = M_* + M_{BH}$ is the total mass and $\mu = \frac{M_* M_{BH}}{M}$ is the reduced mass of the system.

Thus, radiation is emitted in a single spectral line at a frequency $\nu_{orb} = \frac{\omega_{orb}}{2\pi}$, i.e.

$$h_+^{orb}(\nu) = \frac{1}{r} \frac{A}{4\pi} [\delta(\nu - 2\nu_{orb}) - \delta(\nu + 2\nu_{orb})]. \quad (27)$$

Due to gravitational emission the orbit decays; thus the signal we compute using eqs. (25) may not be correct, unless the changes induced on the orbit by the energy lost in GW occur on a timescale much longer than the orbital period, so that we can neglect radiation reaction effects. To check whether this is the case for the orbits we consider, we have computed the

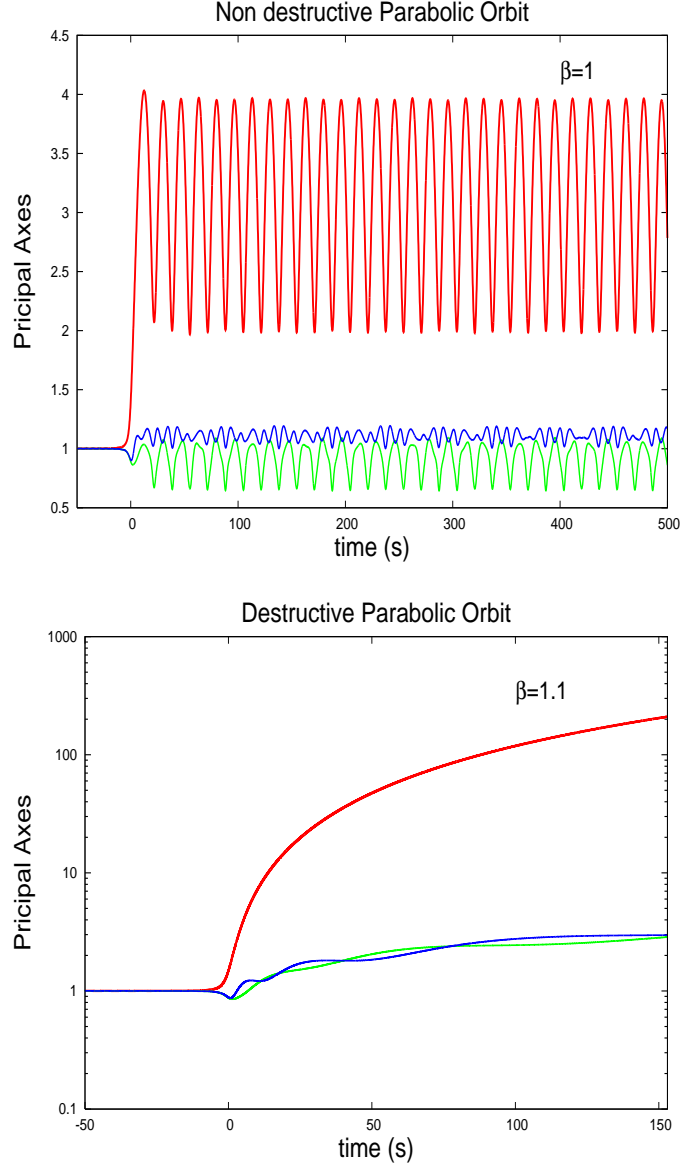


Figure 1. The white dwarf principal axes are plotted versus time for two parabolic orbits with $\beta = 1$ and $\beta = 1.1$. The indefinite growth of one axis in the lower picture signals a destructive interaction.

adiabatic timescale τ

$$\tau \sim \frac{E_{orb}}{L_{GW}}, \quad (28)$$

where $E_{orb} = -\frac{1}{2} \frac{GM\mu}{D}$ is the system orbital energy, and $L_{GW} \equiv \frac{dE_{GW}}{dt}$ is the GW-luminosity due to the time variation of the orbital quadrupole moment

$$L_{GW} = \frac{32 G^4 \mu^2 M^3}{5 c^5 D^5}.$$

The results of our calculations on the tidal interaction are summarized in figure 2 and 3 and in table 2.

Table 2. Orbital parameters and GW signals amplitudes are tabulated for different values of the penetration factor β (column 1) for circular orbits. The orbital radius R , period T and frequency ν_{orb} are given in columns 1 to 4; the adiabatic timescale τ is in column 5; in the last two columns we give the amplitude of the spectral line of the orbital signal, $A/4\pi$, and that of the **f**-mode peak appearing in the tidal signal; they are both multiplied by the source distance, r .

β	R_p 10 ⁴ (km)	T (s)	ν_{orb} (Hz)	τ (s)	$(A/4\pi) \times r$ 10 ⁻⁴ (km)	$h_{max} \times r$ 10 ⁻⁴ (km)
0.15	14.6	336.4	3.0×10^{-3}	4.8×10^{11}	0.46	1.7
0.3	8.0	118.9	8.5×10^{-3}	3.1×10^{10}	0.87	2.7
0.4	6.0	77.2	1.3×10^{-2}	1.0×10^{10}	1.4	4.2
0.5	4.8	55.3	1.8×10^{-2}	4.0×10^9	1.5	7.0
0.6	4.0	42.0	2.4×10^{-2}	1.9×10^9	1.7	9.2
0.7	3.1	33.4	3.0×10^{-2}	1.0×10^9	2.5	15

In the upper panel of figure 2 we plot the Fourier transform of the tidal signal $h_+^{def}(\nu)$ for $\beta = 0.4$. The plot shows a number of very sharp peaks. The first is at $\nu = 2\nu_{orb}$, and it is a signature of the orbital motion on the tidal deformation of the star. The highest peak is at a frequency $\nu_f = 0.146$ Hz, which is the frequency of the fundamental mode of the non radial oscillations of the star in the unperturbed configuration (i.e. when it has a spherical form). This peak is surrounded by equally spaced peaks, at frequencies $\nu = \nu_f \pm 2n\nu_{orb}$, $n = 1, 2, \dots$, due to the coupling of the orbital motion to the deformation. In addition, we also see smaller peaks at the frequencies of the first pressure mode, $\nu_{p_1} = 0.316$, and further harmonics $\nu = \nu_{p_1} \pm 2n\nu_{orb}$. This picture clearly shows that the non radial modes of oscillations of the star are excited in the tidal interaction and their signature appears in the gravitational wave spectrum. The plot for $h_\times^{def}(\nu)$ is entirely similar and will not be shown.

In the lower panel of figure 2 we show $h_+^{def}(\nu)$ for increasing values of β (i.e. for decreasing orbital radii); we see that, as β increases and the orbit shrinks, the $2\nu_{orb}$ - peak shifts toward higher frequencies, but the peaks corresponding to the excitation of the **f**- and **p**-modes, of course, do not move. Moreover, due to the change of ν_{orb} the spacing between the harmonics changes as well.

Finally, in figure 3 we show the signal for the case $\beta = 0.7$ which is close to tidal disruption (see table 1). In this case the contribution of different harmonics is higher, giving rise to a richer structure in the frequency spectrum.

In table 2, for several values of β we show the orbital radius R , period T and frequency ν_{orb} (column 1 to 4); in column 5 we give the adiabatic timescale τ . These data show that,

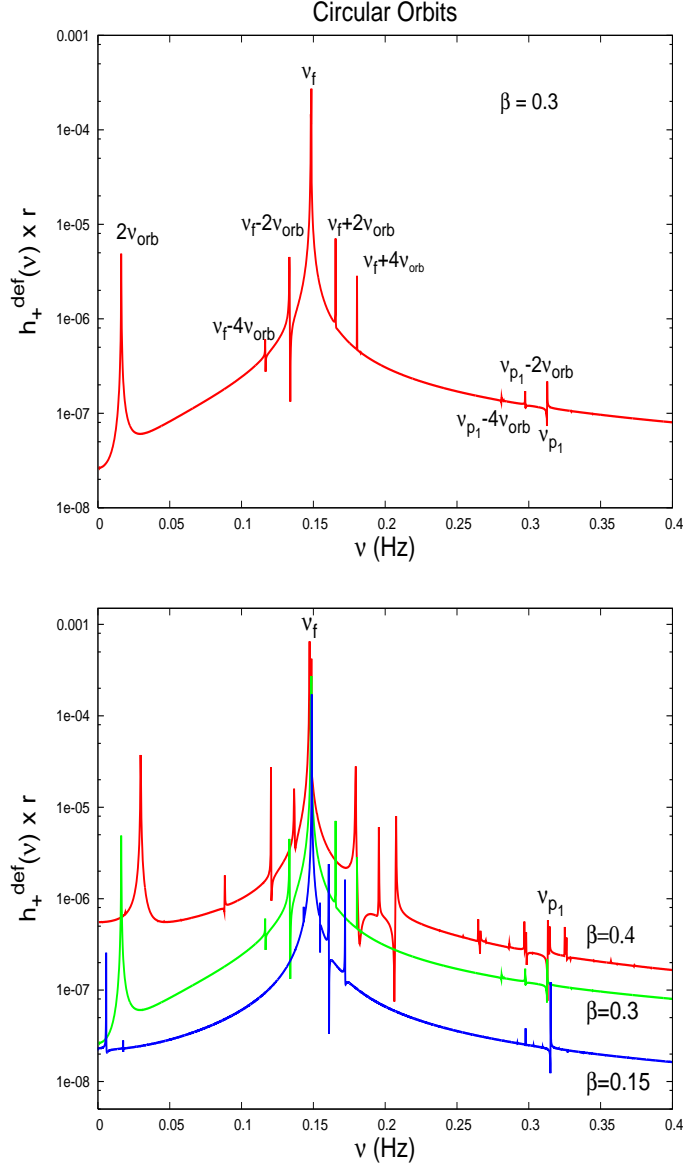


Figure 2. The Fourier transform of the GW signal associated to the tidal interaction between a $1 M_{\odot}$ WD and a $10 M_{\odot}$ BH is plotted as a function of frequency for a circular orbit with $\beta = 0.3$ (up) and for different values of β (down). The main peak at $\nu_f = 0.146$ Hz corresponds to the frequency of the fundamental mode of the non radial oscillations of the star, a smaller peak at $\nu = 0.316$ Hz indicates the excitation of the first \mathbf{p} -mode. The remaining harmonics are due to the coupling between orbital and tidal motion (see text).

for the orbits we consider, we are always in the adiabatic regime since $\tau \gg T$. In the last two column we give the amplitude of the spectral line of the orbital signal, $A/4\pi$, where A is given in eq. (26), and the amplitude of the \mathbf{f} -mode peak appearing in the tidal signal h_+^{def} . It is interesting to note that the \mathbf{f} -mode occurs at frequencies higher than $2\nu_{orb}$, and its amplitude is always larger than that of the orbital signal.

It is worth mentioning that the damping time of the fundamental mode is very large, of the order of $\tau_{GW} \sim 10^6$ seconds for the stars we consider.

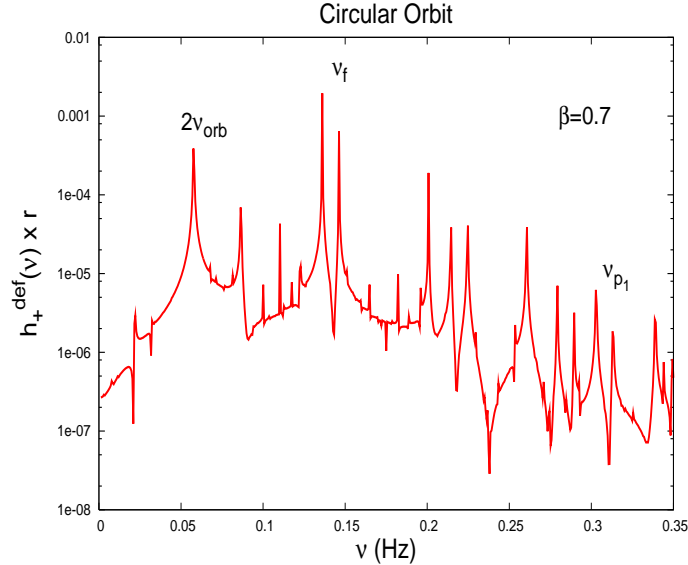


Figure 3. Tidal signal for a circular orbit with $\beta = 0.7$. The coupling between orbital and tidal motion is stronger than in figure 2 (where β is smaller) and higher harmonics are excited.

3.2 Elliptic orbits

Whereas for a circular orbit radiation is emitted in a single spectral line at twice the orbital frequency, when the orbit is eccentric waves are emitted at frequencies multiple of ν_{orb} , and the number of equally spaced spectral lines increases with the eccentricity (Peters & Mathews 1963; Ferrari, D’Andrea & Berti 2000). In the left panel of figure 4 we compare the orbital (up) and the tidal (down) signal emitted on an orbit with $\beta = 0.4$ and $e = 0.75$.

As in the circular case, the excitation of the \mathbf{f} - and \mathbf{p}_1 -modes is manifested by the sharp peaks at the corresponding frequencies, and it is interesting to see that the coupling between the orbital and tidal motion introduces a large number of harmonics. Note also that the maximum of the orbital signal is much larger than the \mathbf{f} -mode peak in tidal signal.

In the right panel of figure 4 we show how the structure of the tidal signal changes due to eccentricity, plotting $h_+^{def}(\nu)$ for $\beta = 0.4$ and for two values of e , (upper panel): as expected, we see that lower eccentricities correspond to a smaller number of spectral lines due to the orbital-tidal coupling. In the same figure (lower panel) we compare the tidal signal emitted on orbits with the same eccentricity ($e = 0.75$) and different values of β , showing how the mode excitation is sensitive to the penetration parameter.

We find that for the orbital parameters tabulated in table 3, the maximum of the orbital signal is always much larger than the \mathbf{f} -mode peak in tidal signal.

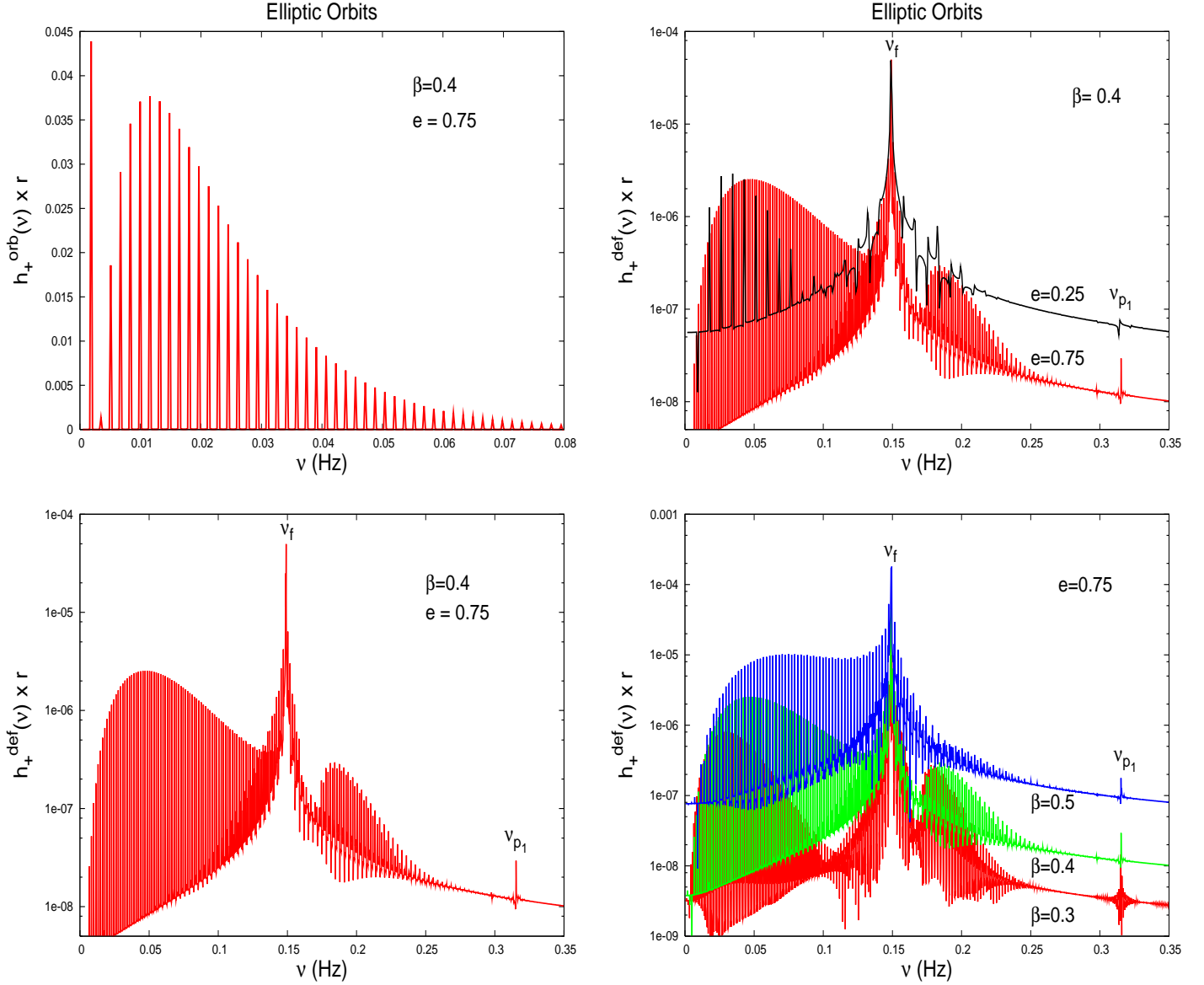


Figure 4. In the left panel we plot the Fourier transform of the orbital signal (up) and of the tidal signal (down) emitted by the WD-BH binary studied in this paper when the orbit is an ellipse with $\beta = 0.4$ and $e = 0.75$. As in the circular case, the main peak in h_+^{def} corresponds to the excitation of the f-mode, but its amplitude is much lower than that of the maximum in h_+^{orb} . In the right panel we show the tidal signal for elliptic orbits with β assigned and varying e (up), and with e assigned and varying β (down).

Table 3. Orbital parameters of the elliptic orbits we consider, plotted for different β (column 1): the eccentricity (column 2), periastron and apoastron distances (column 3 and 4), orbital period (column 5).

β	e	R_p (10^4 km)	R_a (10^5 km)	T (s)
0.4	0.25	6.0	1.0	42
0.3	0.75	8.1	5.6	338
0.4	0.75	6.0	4.2	220
0.5	0.75	4.8	3.4	157
0.6	0.95	4.0	15.7	1337

3.3 Parabolic orbits

While for circular and elliptic orbits the orbital GW-signal has a discrete structure in the frequency domain, parabolic orbits are associated to signals that are continuous functions of ν . As an example, in the left panel of figure 5 we show $h_+^{orb}(\nu)$ and $h_+^{def}(\nu)$ emitted in a parabolic orbit with $\beta = 0.6$. Again, the mode excitation is manifest in $h_+^{def}(\nu)$, and again the orbital and the tidal contributions are in a different frequency range; but now, unlike the circular and elliptic cases, the dominant contribution appears to be the tidal one, reaching a peak-amplitude of about $\sim 10^{-2}$ at $\nu_f = 0.146$ Hz, about twice the amplitude of the orbital peak, which occurs at $\nu = 1.6 \cdot 10^{-2}$ Hz.

Comparing the orbital signal of figure 5 with the orbital signal in figure 4 (upper panel, left) we see that the shape of the parabolic signal is basically the envelope of the elliptic one; indeed, the parabola can be seen as the limiting case of an ellipse with eccentricity equal to unity. It is interesting to compare the signal emitted on the parabolic orbit with that emitted on a very elongated elliptic orbit with the same β : in the right panel of figure 5 we show the orbital (up) and the tidal (down) signals emitted when the orbit is an ellipse with $\beta = 0.6$ and $e = 0.95$. We see that in this case the amplitude of the **f**-mode peak increases significantly with respect to the orbital one, though it does not become bigger. Thus it appears that, for a fixed β , the oscillations modes of the star increasingly contribute to the total emitted radiation as the orbit elongation increases, and become dominant when the orbit is a parabola.

In figure 6 we plot the tidal signal for parabolic orbits for different values of the penetration factor. It should be mentioned that, as for circular and elliptic orbits, the signals emitted along the axis orthogonal to the orbital plane in the ‘ \times ’-polarization have a structure similar to that of the ‘+’-polarization, and for this reason we omit to show them.

As a last example, we have computed the radiation emitted when the star penetrates more deeply into the black hole tidal radius, choosing values of $\beta > 1$, but always lower than the tidal disruption limit. In this case the star is highly deformed and assumes a ‘cigar’ shape; therefore, we cannot expect to see in the frequency spectrum the peaks corresponding to the excitation of the modes of the spherical star, as it was in previous cases.

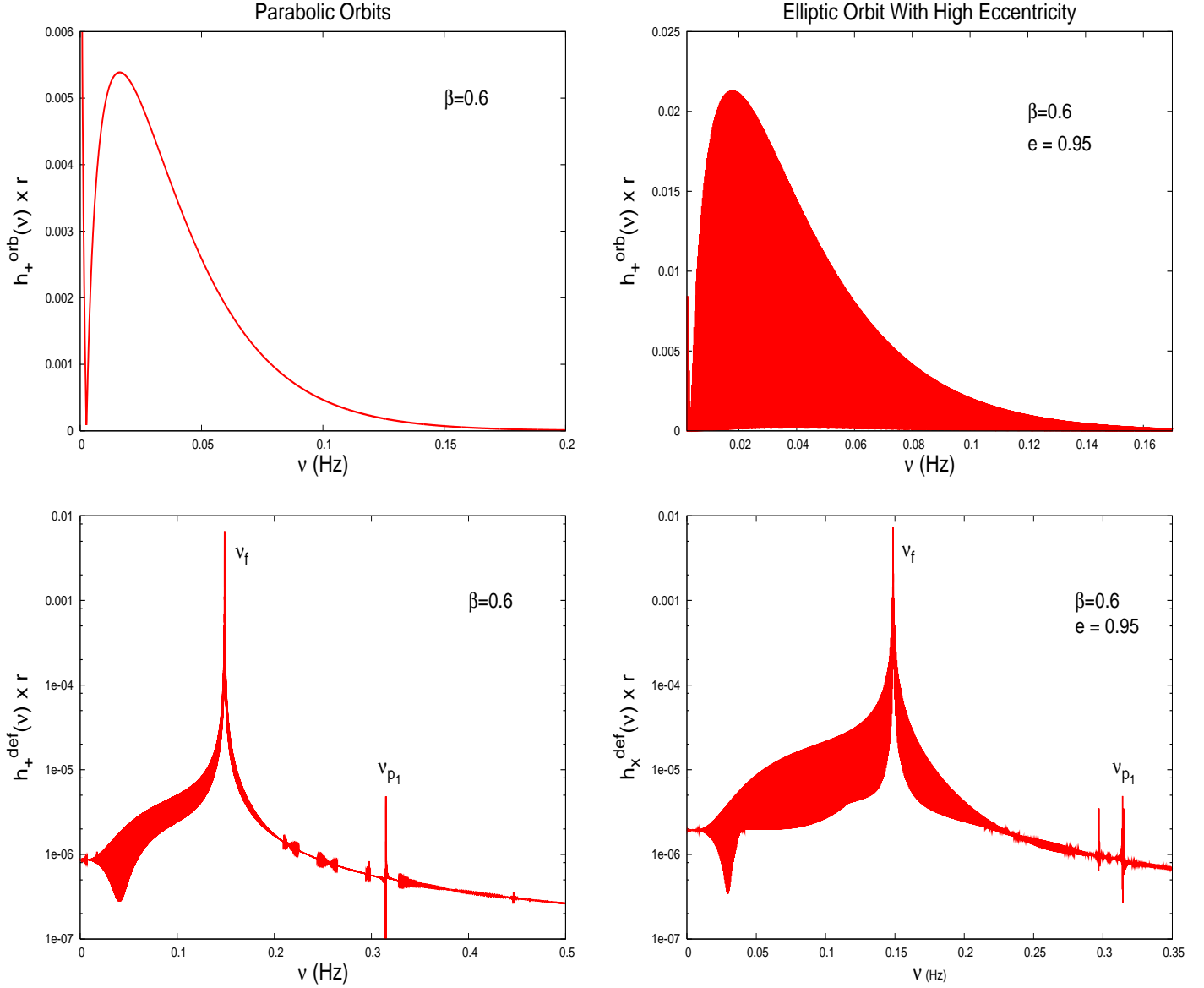


Figure 5. In the left panel we plot the Fourier transform of the orbital signal (up) and of the tidal signal (down) emitted when the WD moves on a parabolic orbit with $\beta = 0.6$. For comparison, in the right panel we show the orbital and the tidal signal when the orbit is elliptic, with the same β and very high eccentricity $e = 0.95$.

However, the cigar also oscillates and his eigenfrequencies scale as the inverse of his length, being the mass fixed. Indeed the tidal signal presents a very interesting structure shown in figure 7. In the three panels on the left we show $h_+^{def}(\nu)$ for $\beta = 1, 1.03, 1.05$. We see that there is a dominant peak which corresponds to the excitation of the fundamental mode of the cigar; indeed, as expected, when β increases the tidal interaction is stronger, the star assumes a more elongated cigar shape and the frequency of the main peak decreases. The spectrum also shows several equally spaced spectral lines and their origin can be understood by looking at the right panel of figure 7, were we plot the principal axes of the star as functions of time.

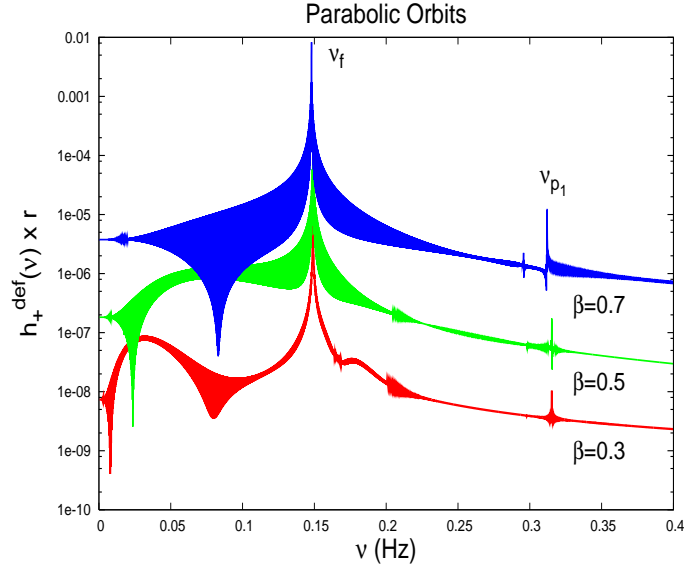


Figure 6. The Fourier transform of the tidal signal emitted in parabolic orbits is plotted as a function of frequency for three values of β .

When the star approaches the black hole, one of the axes on the equatorial plane - let us name it ‘a’- grows much more than the other two, ‘b’ and ‘c’. In the figure the axes are normalized to their initial values, therefore at large distance (large negative time) they are all equal to 1 since the star is spherical. Analysing the axes behaviour, we can identify two characteristic frequencies: one, ν_1 , which corresponds to the first oscillation, when the a-axis starts to grow, reaches the maximum elongation, and then decreases to the value about which it will oscillate in the new, approximately Riemannian, stationary configuration; the second one, ν_2 , corresponds to the oscillation of the a-axis about the new configuration. For the three values of β considered in figure 7 these frequencies are given in table 4. Referring, for example, to the signal $h_+^{def}(\nu)$ for $\beta = 1$ in the left panel of figure 7, and indicating with ν_0 the frequency corresponding to the fundamental mode of the ‘cigar’, we see that there are equally spaced spectral lines at $\nu = \nu_0 \pm n\nu_2$, with $n = 1, 2, \dots$, and smaller peaks (only the first on the left of the main peak is clearly visible) which correspond to $\nu = \nu_0 \pm n\nu_1$. The spacing between the peaks corresponds exactly to the frequencies, given in table 4, at which the axes oscillate.

3.4 Results for a different black hole mass

It is interesting to see how the entire picture discussed above changes if we change the black hole mass. Be R_p the periastron distance (coincident with the orbital radius in the circular case). The tidal tensor (5) scales as $C_{ij} \propto (M_{BH}/R_p^3) = \beta^3$; therefore we expect that, for an

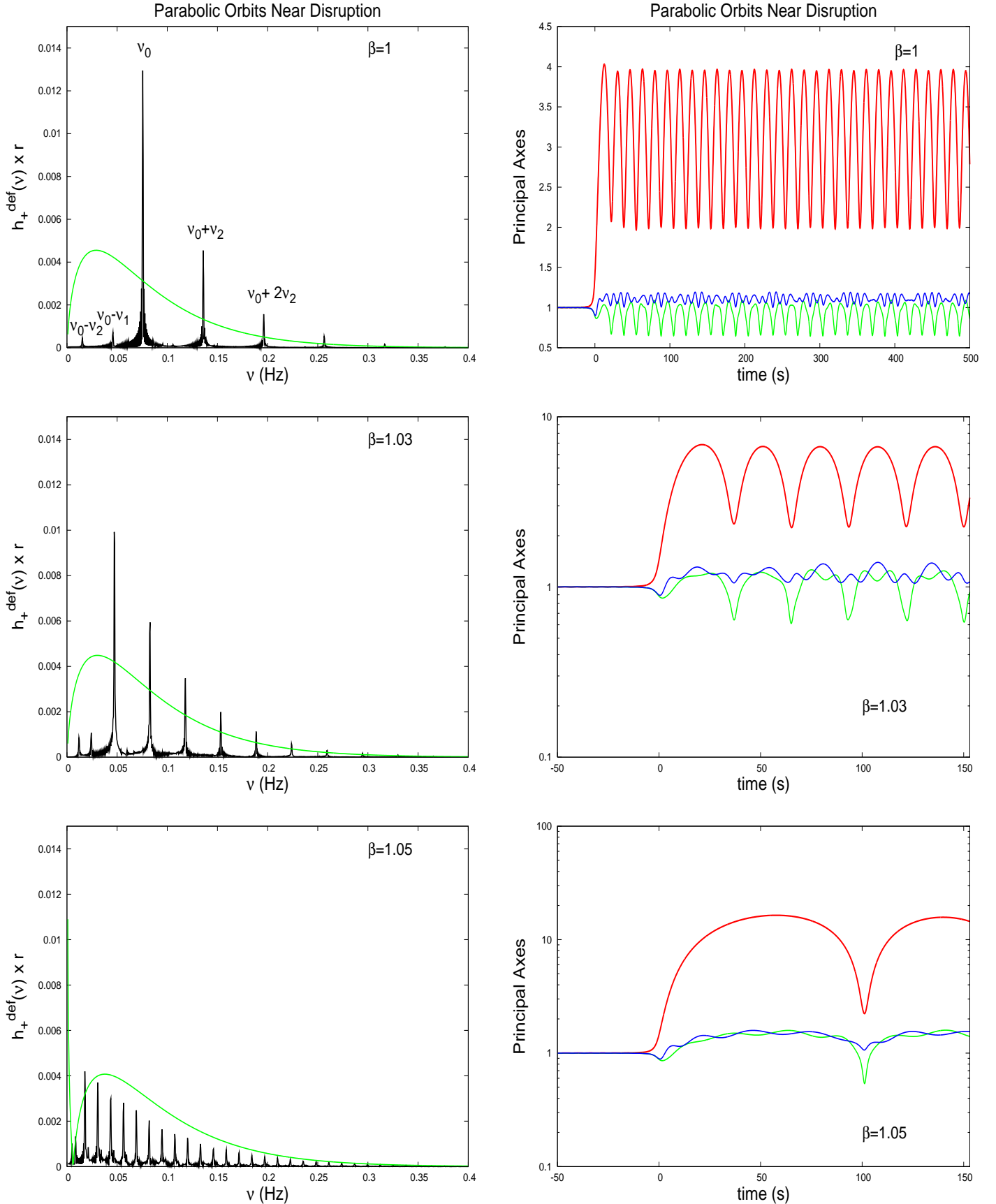


Figure 7. The tidal signal emitted in a parabolic orbit is plotted for three values of β approaching the critical value (left panel). The green continuous line is the orbital signal, plotted for comparison. On the right panel we show the behaviour of the principal axes of the star as a function of time, when the star passes through the periastron. The relation between the axes behaviour and the emitted signal, and the origin of different peaks in h^{def} are explained in the text.

Table 4. In this table we give, for three values of β approaching the critical value and for parabolic orbits, three frequencies characteristic of the tidal deformation: ν_0 , is the frequency of the main peak appearing in the tidal signals shown in figure 7 and corresponds to the excitation of the fundamental mode of the deformed star; ν_1 , refers to the first oscillation of the a-axis as the star approaches the periastron, and ν_2 corresponds to the oscillation of the a-axis about the new cigar-like configuration.

β	ν_0 (10^{-2} Hz)	ν_1 (10^{-2} Hz)	ν_2 (10^{-2} Hz)
1	7.5	4.6	6.0
1.03	4.7	2.5	3.5
1.05	1.8	0.8	1.3

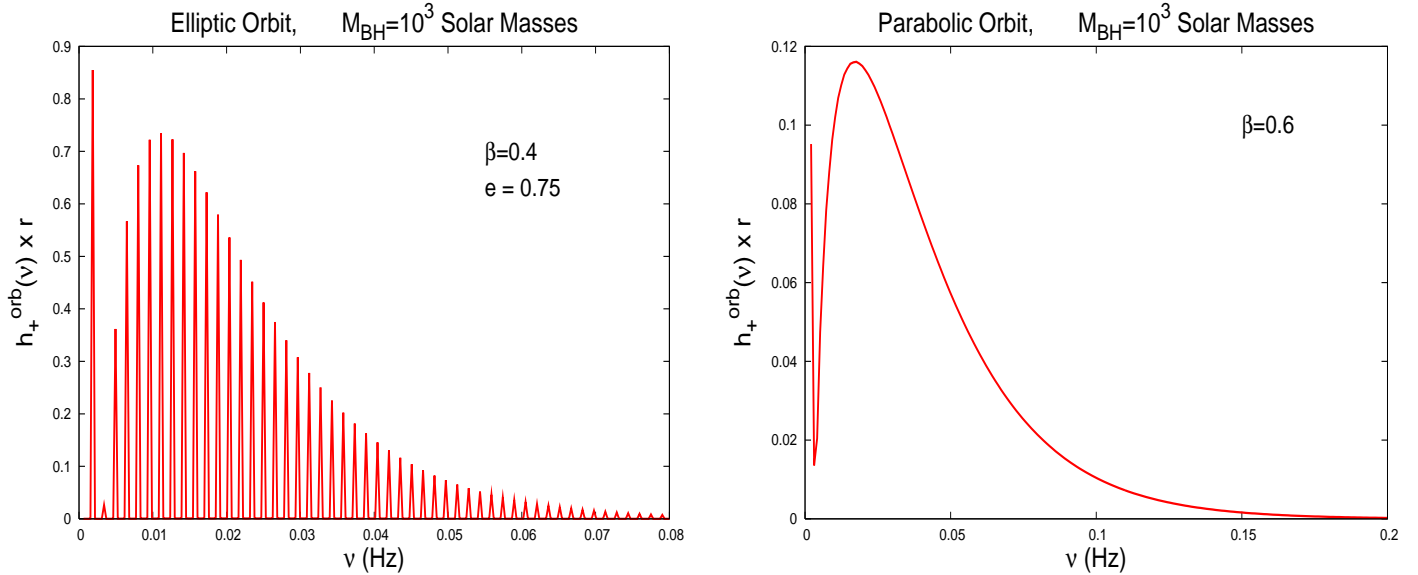


Figure 8. The orbital signal emitted when the black hole mass is $M_{BH} = 10^3 M_{\odot}$ is plotted for an eccentric orbit with $\beta = 0.6$ and $e = 0.75$ (left) and for a parabolic orbit with $\beta = 0.6$ (right). These plots have to be compared to the upper panel of figure 4 and 5, respectively, where the orbital signal is plotted for the same orbital parameters and a black hole mass $M_{BH} = 10 M_{\odot}$.

assigned β , both the tidal signal h^{def} and the critical value of β needed for disruption are independent of the black hole mass. Indeed, this is what we find by numerical integration.

Conversely, the orbital part of the signal, h^{orb} , depends on the black hole mass. For instance, in the circular case from eq. (26) we see that for $M_* \ll M_{BH}$ the amplitude of the emitted spectral line is $A \propto M_{BH}$, showing that the orbital signal increases with M_{BH} . A similar behaviour is exhibited in elliptic and parabolic orbit, as shown in figure 8, where we plot h_+^{orb} emitted when $M_{BH} = 10^3 M_{\odot}$, for an elliptic orbit with $\beta = 0.6$ and $e = 0.75$ (left) and for a parabolic orbit with $\beta = 0.6$ (right). A comparison of these signals with those found for the same parameters when the black hole mass was $M_{BH} = 10 M_{\odot}$ (upper panel, left, of figure 4 and 5, respectively) clearly shows how the orbital signal increases with M_{BH} .

4 CONCLUDING REMARKS

In this paper we have computed the gravitational signal emitted when a white dwarf moves around a black hole on a closed or open orbit. We have computed both the orbital and the tidal contributions and compared the two, assuming that the star is close to the black hole, but in a region safe enough to prevent its tidal disruption. In all cases, the non radial oscillation modes of the star are excited (in our approach we do not include the dynamical behaviour of the black hole) to an extent which depends on how deep in the tidal radius the star penetrates and on the type of orbit. The orbital, h^{orb} , and the tidal, h^{def} , contributions are emitted at different frequencies: smaller for h^{orb} , higher for h^{def} .

The system we have analyzed in detail is composed of a $1 M_{\odot}$ white dwarf and a $10 M_{\odot}$ black hole. In this case we find that for circular orbits up to the critical one, the amplitude of the single spectral line in h^{orb} is always smaller than that of the **f**-mode peak in h^{def} ; however if the black hole mass is larger, the situation reverses, since h^{def} is nearly independent of M_{BH} , while h^{orb} is proportional to it. It is interesting to note that h^{def} contains several peaks that shows the coupling between the orbital and tidal motion.

When the orbit is elliptic, h^{orb} shows several spectral lines emitted at multiples of the orbital frequency; h^{def} has again a main peak at the **f**-mode frequency, and in addition a number of peaks due to the orbital-tidal interaction, that contain a signature of the nature of the orbit. The amplitude of the **f**-mode peak of course increases with the penetration factor β and also, for a fixed β , with the eccentricity; for the system we have considered this amplitude tends to that of the maximum of h^{orb} for very elongated orbits ($e > 0.95$). Again changing the black hole mass to a higher value the orbital contribution increases with respect to the tidal one.

For parabolic orbits the situation is very interesting, since the star can penetrate more deeply into the tidal radius, allowing for larger values of β . As β tends to the critical value the star assumes a very elongated, cigar-like shape, deviating considerably by its initial spherical structure. Thus the main peak in h^{def} shifts toward lower frequencies, since the **f**-mode frequency scales as the inverse of the length of the principal axis. The harmonics which appear in the tidal signal correspond to the oscillation frequencies of the principal axis of the ‘cigar’, and the larger is β the higher will be the number of excited harmonics. A comparison with the behaviour of the orbital signal (see figure 7) shows that if $\beta < 1.03$

the tidal signal is considerably higher than h^{orb} if $M_{BH} = 10 M_{\odot}$, but again the situation reverses if the black hole mass is sufficiently higher.

The results of our study show that the tidal signals emitted by a close encounter between a white dwarf and a black hole lay in a frequency region which is intermediate between the sensitivity region of LISA ($10^{-4} - 10^{-1}$ Hz) and that of ground-based interferometers VIRGO, LIGO, GEO, TAMA, sensitive above ~ 10 Hz. Detectors that fill this gap have recently been proposed, like the Big Bang Observatory, thought as follow on mission to LISA (Bender *et al.* 2005), and DECIGO, proposed by a Japanese group (Seto, Kawamura & Nakamura 2001); they should both be extremely sensitive in the decihertz region $10^{-1} - 1$ Hz, and would be the appropriate instruments to detect the tidal signals we have studied and to shed light on the dynamics of dense stellar clusters where these processes are more likely to occur.

Acknowledgements

We would like to thank L. Rezzolla for introducing us to the literature on the subject, and L. Gualtieri for useful conversations and fruitful insights in various aspects of the work.

REFERENCES

- Bender P.L., Armitage P.J., Begelman M.C., Perna R., iper submitted to the NASA SEU Roadmap Committee
 Berti E., Ferrari V., 2001, Phys. Rev. D, 63, 064031
 Bicknell G.V., Gingold R.A., 1983, ApJ, 273, 749
 L. Blanchet, Living Reviews of Relativity Irr-2002-3, (<http://www.livingreviews.org/>) 2002
 Carter B., 1992, ApJ, 391, L67
 Carter B., Luminet J.P., 1982, Nature, 296, 211
 Carter B., Luminet J.P., 1983, A&A, 121, 97
 Carter B., Luminet J.P., 1985, MNRAS, 212, 23
 Diener P., Kosovichev A.G., Kotok E.V., Novikov I.D., Pethick C.J., 1995, MNRAS, 275, 498
 Diener P., Frolov V.P., Khokhlov A.M., Novikov I.D., Pethick C.J., 1997, ApJ, 479, 164
 Evans C.R., Kochanek C.S., 1989, ApJ, 346, 13
 Ferrari V., D'Andrea M., Berti E., 2000, Int. J. Mod. Phys. D, 9 n. 5, 495
 Frolov V.P., Khokhlov A.M., Novikov I.D., Pethick C.J., 1984, ApJ, 432, 680
 Fryer C.L., Woosley S.E., Herant M., Davies M.B., 1999, ApJ, 520, issue 2, 650
 Gomboc A., Cadez A., 2005, ApJ, 625, 278
 Gualtieri L., Berti E., Pons J.A., Miniutti G., Ferrari V., 2002, Phys. Rev. D, 64, 104007
 Ivanov P.B., Novikov I.D., 2001, ApJ, 549, 467
 Ivanov P.B., Chernyakova M.A., Novikov I.D., 2003, MNRAS, 338, 147
 Khokhlov A., Novikov I.D., Pethick C.J., 1993, ApJ, 418, 163
 Khokhlov A., Novikov I.D., Pethick C.J., 1993, ApJ, 418, 181
 Kochanek C.S., 1992, ApJ, 385, 604

- Kochanek C.S., 1992, *ApJ*, 398, 234
- Komossa S., Halpern J., Schartel N., Hasinger G., Santos-Lleo M., Predehl P., 2004, *ApJ*, 603, L17
- Kosovichev A.G., Novikov I.D., 1992, *MNRAS*, 258, 715
- Laguna P., Miller W.A., Zurek W.H., Davies M.B., 1993, *ApJ*, 410, 83
- Lai D., Rasio F.A., Shapiro S.L., 1993, *ApJ Suppl.*, 88, 205
- Lai D., Rasio F.A., Shapiro S.L., 1994, *ApJ*, 423, 344
- Lai D., Rasio F.A., Shapiro S.L., 1994, *ApJ*, 437, 742
- Lai D., Shapiro S.L., 1995, *ApJ*, 443, 701
- Luminet J.P., Marck J.-A., 1985, *MNRAS*, 212, 57
- Luminet J.P., Carter B., 1986, *ApJ*, 61, 219
- Luminet J.P., Pichon B., 1989, *A&A*, 209, 85
- Luminet J.P., Pichon B., 1989, *A&A*, 209, 103
- Marck J.-A., 1983, *Proc. R. Soc. of London*, 385, 431
- Marck J.-A., Lioure A., Bonazzola S., 1996, *A&A*, 306, 666
- Novikov I.D., Pethick C.J., Polnarev A.G., 1992, *MNRAS*, 255, 27
- Ogawaguchi W., Kojima Y., 1996, *Prog. Theor. Phys.*, 96, 901
- Peters P.C., Mathews J., 1963, *Phys. Rev.* 131, 435
- Pons J.A., Berti E., Gualtieri L., Miniutti G., Ferrari V., 2002, *Phys. Rev. D*, 65, 104021
- Press W.H., Teukolsky S.A., 1977, *ApJ*, 213, 183
- Rasio F.A., Shapiro S.L., 1995, *ApJ*, 438, 887
- Schodel R., Ott T., Genzel R., Hofmann R., Lehnert M., Eckart A., Mouawad N., Alexander T., Reid M.J., Lenzen R., Hartung M., Lacombe F., Rouan D., Gendron E., Rousset G., Lagrange A.M., Brandner W., Ageorges N., Lidman C., Moorwood A.F.M., Spyromillio J., Hubin N., Menten K.M., 2002, *Nature*, 419, 694
- Shibata M., Uryu K., 2001, *Phys. Rev. D*, 64, 104017
- Seto N., Kawamura S., Nakamura T., 2001, *Phys. Rev. Lett.*, 87, 221103
- Wiggins P., Lai D., 2000, *ApJ*, 532, 530